1
2
3
4
Surface Observation Constrained High Frequency Coal Mine Methane Emissions in Shanxi China Reveal More Emissions than Inventories, Consistency with Satellite Inversion

5 Fan Lu[1], Qin Kai[1*], Jason Blake Cohen[1*], Qin He[1], Pravash Tiwari[1], Wei Hu[1], Chang

6 Ye[1], Yanan Shan[1], Qing Xu[1], Shuo Wang[1], Qiansi Tu[2]

7 [1]Jiangsu Key Laboratory of Coal-Based Greenhouse Gas Control and Utilization, School of Environment

8 and Spatial Informatics, China University of Mining and Technology, Xuzhou, China

9 [2]School of Mechanical Engineering, Tongji University, Shanghai, China

10 *Correspondence to*: Kai Qin (qinkai@cumt.edu.cn) ; Jason Blake Cohen (jasonbc@alum.mit.edu)

11 **Abstract.** This work focuses on Changzhi, Shanxi China, a city and surrounding rural region with one

12 of the highest atmospheric concentrations of methane (CH_4) world-wide (campaign-wide

13 minimum/mean/standard deviation/max observations: 2.0, 2.9, 1.3, and 16 ppm) due to a rapid increase

14 in the mining, production, and use of coal over the past decade. An intensive 15-day surface observation

15 campaign of CH_4 is used to drive a new analytical, mass-conserving method to compute and attribute

16 CH_4 emissions. Observations made in concentric circles at 1km, 3km, and 5km around a high production

17 high gas coal mine yielded emissions of 0.73, 0.28, and 0.15 ppm min^{-1} respectively. Attribution used a

18 2-box mass conserving model to identify the known mine's emissions from 0.042-5.3 ppm min^{-1}, and a

19 previously unidentified mine's emission from 0.22-7.9 ppm min^{-1}. These results demonstrate the

20 importance of simultaneously quantifying both the spatial and temporal distribution of CH_4 to better

21 control regional-scale CH_4 emissions. Results of the attribution are used in tandem with observations of

22 boundary layer height to quantify policy-relevant emissions from the two coal mines as 13670±7400 kg

23 h^{-1} and 5070±2270 kg h^{-1} respectively. Both mines display a fat tail distribution, with respective 25th,

24 median, and 75th percentile values of [870, 7500, 38700] kg h^{-1} and [431, 1590, 7000] kg h^{-1}. These

25 findings are demonstrated to be higher than CH_4 emissions from equivalent oil and gas operations in the

26 USA, with one about double and the other similar to day-to-day emissions inverted over 5-years using

27 TROPOMI over the same region.

28
29
30

1. Introduction

31

32   Emissions of Methane (CH_4) contribute the second most to direct anthropogenic longwave radiative

33   forcing (Etminan et al., 2016; Li et al., 2022). Since CH_4 has a lifetime from 9.5 to 12.5 years (Li et al.,

34   2022; Prather et al., 2012), controlling CH_4 emissions can provide an opportunity to mitigate peak

35   loading and slow the rate of net global warming. Fossil fuel CH_4 is one of the largest sources of

36   anthropogenic CH_4 emissions (Kirschke et al., 2013; Saunois et al., 2020a). Since China is the world's

37   largest producer and consumer of coal (Bournazian, 2016), Coal mines CH_4 (CMM) possibly contributes

38   up to 33%-40% of China's total CH_4 emissions (Janssens-Maenhout et al., 2017; Miller et al., 2019; Peng

39   et al., 2016). Although China enacted CMM regulations in 2010, CMM continues grow (Kerr and Yang,

40   2009; Miller et al., 2019). CH_4 emission estimates are highly uncertain in both space and time (Brandt et

41   al., 2014; Saunois et al., 2020b). They also generally have a fat tail distribution, wherein a small number

42   of samples have extremely large emissions that overwhelm emissions under average conditions (Duren

43   et al., 2019; Plant et al., 2022). For these reasons, new approaches to quantify, reduce uncertainty, and

44   attribute CH_4 emissions are necessary and can provide support for policies aiming to control and mitigate

45   CMM (Cao, 2017).

46   Bottom-up (BU) quantification of emissions requires a priori knowledge of source locations and

47   diversity, which tends to not represent real-world conditions. Top-down (TD) approaches analyze

48   concentration data with improving accuracy (Allen, 2014; Rigby et al., 2019; Varon et al., 2018; Vaughn

49   et al., 2018), specifically combining surface (Heerah et al., 2021; Katzenstein et al., 2003; Shi et al.,

50   2023), aircraft (Karion et al., 2013; Shi et al., 2022; Tong et al., 2023; Vinković et al., 2022), and/or

51   satellite (Wecht et al., 2014) CH_4 observations with atmospheric models. Some TD approaches use

52   physically realistic but complex chemical transport models (Bloom et al., 2017) , others use plume

53   models (Goldsmith et al., 2012), and others still use data driven approaches (Buchwitz et al., 2017).

54   Uncertainties are rarely assessed holistically or in detail (Cohen and Prinn, 2011; Cohen and Wang, 2014).

55   Airborne remote sensing is a highly technical and costly approach to record CH_4 fluxes from

56   landfills, coal basins, and oil and gas production (Krautwurst et al., 2021; Krautwurst et al., 2017;

57   Kuhlmann et al., 2023), which suffers from not being able to monitor CH_4 emissions over long periods

58   of time or in regions where the source is not well constrained (Brandt et al., 2014; Gorchov Negron et

59   al., 2020; Hiller et al., 2014; Mehrotra et al., 2017; Molina et al., 2010). Satellite remote sensing can

60   measure CH_4 under specific orbits where the source is known and identified (Jacob et al., 2016; Jacob et

61   al., 2022; Plant et al., 2022; Varon et al., 2018; Zhang et al., 2020), but only after being calibrated by

62   upward looking remotely sensed measurements (Tu et al., 2022), and only when the atmosphere is rain,

63   cloud and aerosol free (Cohen and Prinn, 2011; Reuter et al., 2019; Sadavarte et al., 2021). TROPOMI

64   and GOSAT have both been shown to be data-rich at times (Butz et al., 2012; Hu et al., 2018; Jacob et

65   al., 2016), but severely limited at other times (Butz et al., 2012; Kuze et al., 2009). Even when these

66   satellites have sufficient data to compute emissions from other species, frequently CH_4 cannot be

67   computed (Li et al., 2023; Qin et al., 2023b) due to insufficient signal strength, and uncertainties which

68   are both non-understood and mis-constrained (Povey and Grainger, 2015).

69   Ground-based remote sensing provides higher accuracy versus satellite observations (Heerah et al.,

70   2021; Luther et al., 2022; Tu et al., 2022). EM27/SUN measurements have approximated CH_4 emissions

71   in Poland (Luther et al., 2019; Luther et al., 2022). However, these instruments are expensive, require

72   calibration, and have limited data collection due to solar signal strength.

73   This work employs a high-frequency surface-based observation platform of CH_4 concentration

74   which is portable, economical, and unaffected by most environmental factors. The observations are

75   combined with a new mass-conserving methodology based on temporal transformation of the spatially

76   derived mass-conserving framework successfully applied to NO_2 (Li et al., 2023; Qin et al., 2023b). This

77   work focuses on Shanxi, one of the densest coal mining regions in the world, accounting for

78   approximately 10% of total global coal production (Lin and Liu, 2010; Qin et al., 2023a). Continuous

79   observations were made around known coal mines, unknown sources, and of background conditions.

80   High-frequency emissions calculated using these data were used to drive a 2-box model to attribute

81   emissions to the known mine and a second low production mine previously thought insignificant. The

82   results provide insights into the spatial distribution of CH_4 emissions, demonstrate rapid adoption of

83   practical methods globally, and enable source attribution.

84   **2. Methods and Data**

85   **2.1 Study Site and Campaign Design**

86   Changzhi, Shanxi is located in a basin, with coal mines densely distributed throughout both flat

87   central regions and around the mountainous edges (Figure 1), many of which are classified as high CH_4

88   emitting mines. Due to this combination, province-wide background CH_4 concentrations are very high

89   and have large variation in time. This study mainly focuses on two coal mines: one mine is classified as

90 having high amounts of CH_4 per unit of production and an annual coal production of 4 million tons (CM-

91 A), and the other is unclassified for CH_4 per unit of production and having an annual coal production of

92 3 million tons (CM-B) (Qin et al., 2023a). Observations were positioned along concentric circles located

93 1km, 3km, and 5km from CM-A, over an approximation of the four ordinal directions: east, west, south,

94 north (Figure 2). All locations were planned to be far away from known anthropogenic sources, leading

95 to a net total 12 measurement points. As later discovered, CM-B is located approximately 1km southwest

96 from the measurement point located at 5km west.

97
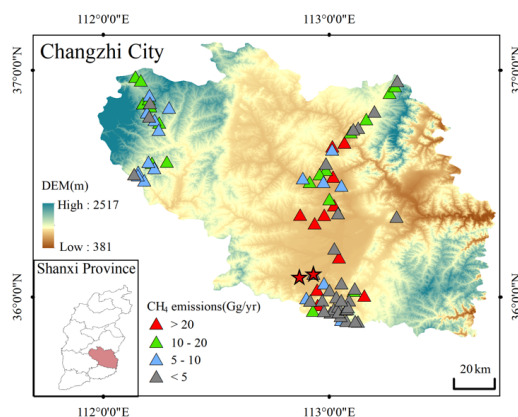
Figure 1. Topographic map of Changzhi, and its location in Shanxi Province (bottom left). The triangles
represent the locations of all individual coal mines (including underground and abandoned mines), where the
triangle color represents the emissions amount: high (red), middle (green), low (blue), and very-low (grey).
The red stars represent the two coal mines in this work.

102
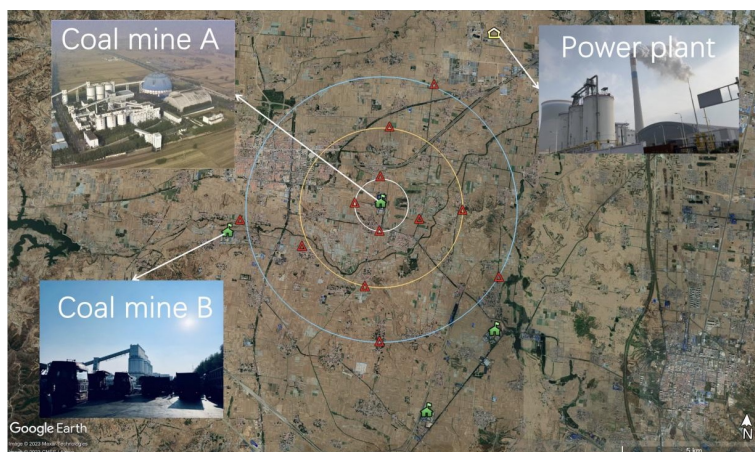
Figure 2. Locations of four individual coal mines (Green filled houses), a power plant (Yellow outlined house),
and the 12 observation locations presented in this work (red double-outlined triangles). Distance from CM-A

105   **are given as concentric circles at 1km (white), 3km (yellow), and 5km (blue).**

106   **2.2 Measuring CH₄ concentration**

107   Atmospheric CH_4 concentrations at 5m above the surface were observed daily at 1 Hz from 8:30 to

108   17:00 local time in August 2022 using two portable greenhouse gas analyzers (LGR-915-0011, California,

109   USA). Three different locations (1 km, 3 km and 5 km) were selected daily along a single direction from

110   the CM-A, allowing a more consistent and precise calculation of the spatial gradient (Table 1). In order

111   to reduce the time errors, using two portable greenhouse gas analyzers randomly selecting the three

112   observation points during the daily measurements and without fixed sequence.

113   The CH_4 data was averaged minute-by-minute to match observed wind data, and subsequently used

114   to compute CH_4 emissions. As show in Figure 3, the CH_4 concentration data is highly correlated with

115   rapid changes in both the wind speed and direction.

116   **Table 1. Detailed Information Summarizing the Dates, Times, and Locations Observed in the Field**

Date	Direction of measured site	Sample period (min)		
		1 km	3 km	5 km
10 August 2022	North	88	35	47
12 August 2022	North	78	66	61
13 August 2022	North	168	181	178
14 August 2022	North	125	128	122
15 August 2022	North	121	122	119
17 August 2022	North, West	122, 124	119, 120	120, 117
18 August 2022	North, West	143, 119	135, 118	125, 120
19 August 2022	East	126	139	140
21 August 2022	North	140	127	125
22 August 2022	East, South	129, 123	124, 133	121, 124
23 August 2022	South	126	129	129

117   Observations made in clean locations with a wind direction not from the mine are subsequently

118   considered for background sites. The lowest and least variable CH_4 observations are found on August 23

119   in the south (2.08±0.08 ppm) (Figure 3). It is important to note that although this site has the minimum

120   concentrations observed in this work, these values are significantly higher than the global latitude-band

121   background. Three other locations and days were observed with relatively low mean and not significantly

122   large variation: August 19 in the east (2.63±0.35 ppm), August 22 in the east (2.65±0.51 ppm), and

123   August 22 in the south (2.60±0.55 ppm) (Figure 3). These results imply that the practice adopted by the

124   community to separate a plume from the global latitude band or climatological background state is not

125   applicable in the locations sampled in this paper (Buchwitz et al., 2017; Irakulis-Loitxate et al., 2021;

126   Lauvaux et al., 2022; Sadavarte et al., 2021). For this reason, a new quantitative approach is presented

127   to understand and quantify what is actually a source and what is not. This approach is applicable under

128   conditions both encountered globally as well as those under the uniquely high and variable conditions

129   observed herein.
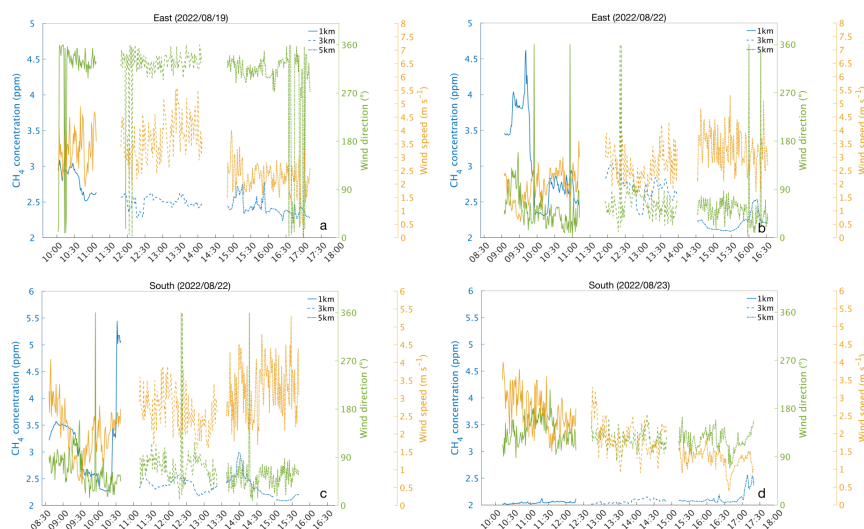
Figure 3. Time series of CH$_4$ concentration (ppm) (blue), wind speed (m s^{-1}) (yellow) and wind direction [º] (orange lines) measured at 1km (solid), 3km (dashed) and 5km (dash-dot) located east (top) and south (bottom) of CM-A on three different days.

2.3 Meteorological Data

135   The wind speed and direction were obtained from local meteorological stations with a temporal

136   frequency of 1min. As show in Figures 4 and 5 the overall wind was dominated by a southerly direction

137   (38.0% of observations between 150° and 210°) and found to be moderately slow (69.9% of observations

138   were between 1 m s^{-1} and 4 m s^{-1}). The 10th and 90th percentiles of wind direction (54° and 312°) and

139   wind speed (1 m s^{-1} and 5.1 m s^{-1}) respectively, indicate that high frequency sampling reveals a small

140   number of relatively large changes are observed, which are expected to lead to a "fat-tail" type of

141   distribution of subsequently computed CH$_4$ emissions (Delkash et al., 2016).

142   The temperature and pressure data were measured by a handheld meteorological instrument

143   (HWS1000, ZOGLAB, China) with a temporal frequency of 1min. The boundary layer data were

144   obtained from https://zenodo.org/records/6498004 (Guo et al., 2022) based on a merging of reanalysis

145   data with observations (Guo et al., 2024).

6
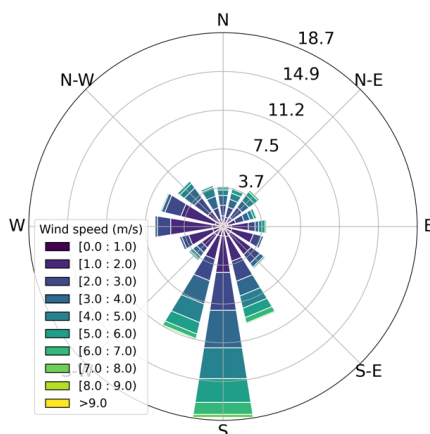
Figure 4. The wind rose of all observed wind speeds from August 10, 2022 to August 25, 2022.
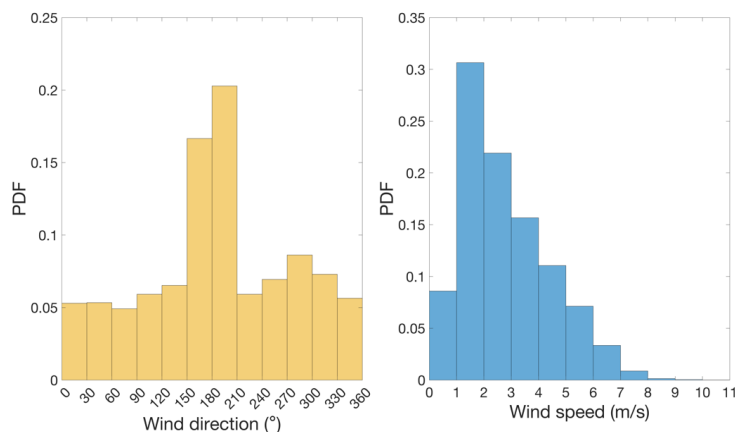
Figure 5. Probability density function (PDF) for all observed wind direction (yellow) and wind speed (blue) from August 10, 2022 to August 25, 2022.

2.4 Quantitative Estimation of CH₄ Emissions

A mass conserving approach was used to estimate the CH₄ emissions in connection with the high frequency observations of CH₄ and meteorological data, hereafter called the Mass Conserving Model of Measured CMM (MCM²). This approach is based on previous dynamic emissions estimates of tropospheric atmospheric column observations of short-lived NO_2 (Li et al., 2023; Qin et al., 2023b), but has never been applied to surface observations in general, or CH₄ in specific. Adopting this approach to solve for CH₄ is done starting with the continuity equation for the conservation of mass (Equation 1), reorganizing the individual terms and converting coordinates from space to time (Equation 2) and finally combining the terms (Equation 3) as follows:

$$\frac{\partial CH_4}{\partial t} = E_{CH_4} - \nabla(U \times CH_4) \quad (1)$$

$$\nabla(U \times CH_4) = CH_4 \times \nabla U + U \times \nabla CH_4 = \alpha \times \left(CH_4 \times \frac{\partial U}{\partial t} + U \times \frac{\partial CH_4}{\partial t}\right) \quad (2)$$

7

162
$$\frac{\partial CH_4}{\partial t} = E_{CH_4} - \alpha \times \left(CH_4 \times \frac{\partial U}{\partial t} + U \times \frac{\partial CH_4}{\partial t} \right) \quad (3)$$

163 where CH_4 is the CH_4 concentration (ppm), t is the time (min), E_{CH_4} is the CH_4 emissions flux (ppm min^{-1}

164 ^{1}), and U is the wind speed (m s^{-1}). The ∇ is a mathematical operator that takes the gradient on spatially

165 distributed variables. However, when considering motion along one-dimension, the relationship between

166 distance, speed, and time can be used to rewrite the spatial derivatives of $\nabla(CH_4)$ and $\nabla(U)$ as temporal

167 derivatives (Brasseur and Jacob, 2017), where α is a conversion coefficient between distance and wind

168 speed.

169   The gradient term used in these equations take into account the local topography of Shanxi, which

170 is known for its significant features and surrounding mountains. These geographical features can impact

171 the transport and dispersion of CH_4, and their effects are incorporated into the wind field in the continuity

172 equation. Notably, when dealing with a non-divergent wind field, the gradient term simplifies to the term

173 $(U \times \nabla CH_4)$ (Sun, 2022). Uncertainty analysis was conducted before calculating the CH_4 emissions to

174 ensure only reliable data was used, since observed variation of CH_4 over time is influenced not only by

175 CH_4 emissions, but also changes in wind speed and pressure. Specifically, $CH_4 \times \frac{\partial U}{\partial t}$ represents the

176 change in CH_4 influenced by pressure, while $U \times \frac{\partial CH_4}{\partial t}$ represents the change in CH_4 influenced by

177 advection. Furthermore, since there is uncertainty in the observations, this work takes a conservative

178 approach, and only considers data when the threshold given by equation (4) is observed to be considered

179 influenced by emissions (a lower threshold can be selected like 25% or 15% et al., but uncertainty will

180 increase).

181
$$u \times \frac{\partial CH_4}{\partial t} / \nabla(U \times CH_4) > 30\% \quad (4)$$

182 The remaining data (approximately 22%, presented as red circle indicators in Figure 6) is not processed

183 in the emissions calculation as the signal is most likely due to a combination of observational uncertainty

184 and white noise (Prinn et al., 1987).
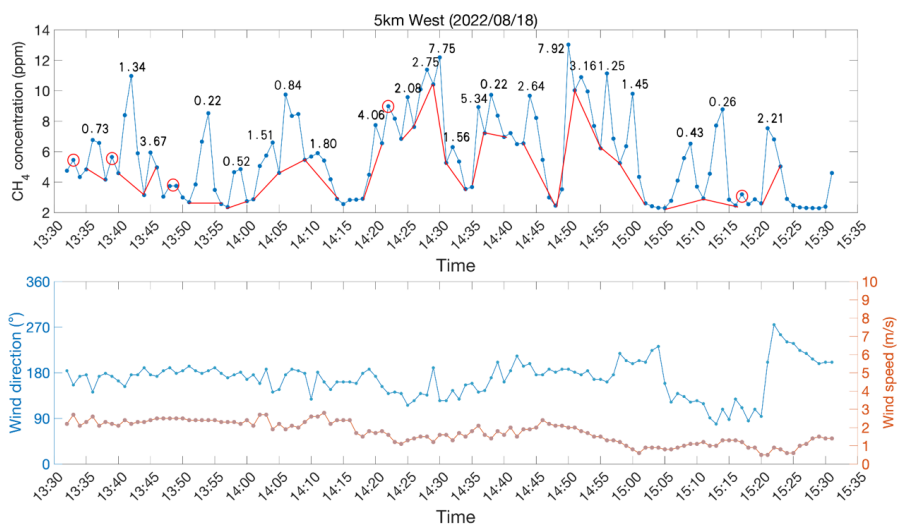
Figure 6. Time series of CH$_4$ concentrations (top, blue), background concentrations (top, red), wind direction (bottom, blue) and wind speed (bottom, red) measured 5km west of CM-A on August 18, 2022. MCM^2 computed CH$_4$ emissions (top, numbers) (ppm min^{-1}) are computed for all regions where the observations are enhanced compared with the background for at least 3 consecutive observations, and which further pass the noise threshold (Equation 4).

2.5 Uncertainty Analysis

In order to reduce the uncertainty of the CH$_4$ emission estimation, only data above the threshold given by equation (4) is consided. Prior to this, uncertainty analysis was also conducted on the relevant variables in actual experiments. As shown in Figure 7, a 5% uncertainty was assigned to both the CH$_4$ concentration and wind speed data, and the CH$_4$ emission flux was calculated. The uncertainty analysis results indicate that probability distribution of all possible calculated emissions are consistent, and the errors are smaller than 5% in each case, consistent with Equation 3 leading to a dampening of the uncertainty, as also observed in Qin et al. (2023a) study. Therefore, we believe that the results of CH$_4$ emissions in this study can be trusted.
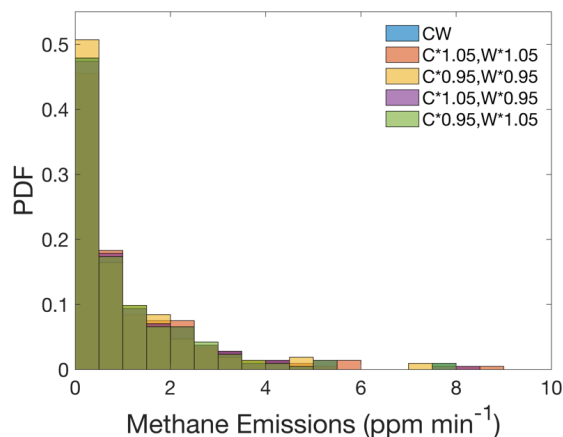
Figure 7. The PDFs of uncertain analysis results (C represents concentration, W represents wind speed).

2.6 Attribution Analysis

A 2-box mass conserving model (based on equation 5) was used to attribute CH$_4$ emissions from the more than one suspected source of CH$_4$ in the 5k west. The changes in CH$_4$ over time t (min) at the observation point $C_{coal\ mine}$ (ppm) is driven by emissions from the upwind coal mine $E_{coal\ mine}$ (ppm min^{-1}) and the concentration gradient computed using the wind U (m s^{-1}), and the background concentration $C_{background}$ (ppm) as demonstrated in Figure 8.

$$\frac{\partial C_{coal\ mine}}{\partial t} = E_{coal\ mine} + U \times C_{background} - U \times C_{coal\ mine} \qquad (5)$$

All observed data points and computed emissions are used when wind direction is capable of transporting the CH$_4$ from either CM-A or CM-B towards the observation site (Figure 8), while the remaining data is not used. A discretized version of Equation 5 is given in Equation 6 and solved using a first order finite difference approach:

$$C_{Coal\ mine_{\tau i+1}} - C_{coal\ mine_{\tau i}} = E_{coal\ mine_{\tau i}} + U_{\tau i} \times C_{background_{\tau i}} - U_{\tau i} \times C_{coal\ mine_{\tau i}} \qquad (6)$$

where τ_i and τ_{i+1} are the current and next time step, and the other terms are defined as in equation 5.

All possible sets of steady-state concentrations are computed using all possible combinations of emissions and concentrations as boundary and initial conditions and running the equation forward to equilibrium. The computed concentrations are analyzed probabilistically by comparing the modeled CH$_4$ probability density function (PDF) with the observed CH$_4$ PDF. Differences between the PDFs are clearly associated with the different wind directions and hence geophysical locations of the sources can be distinguished.

10

221
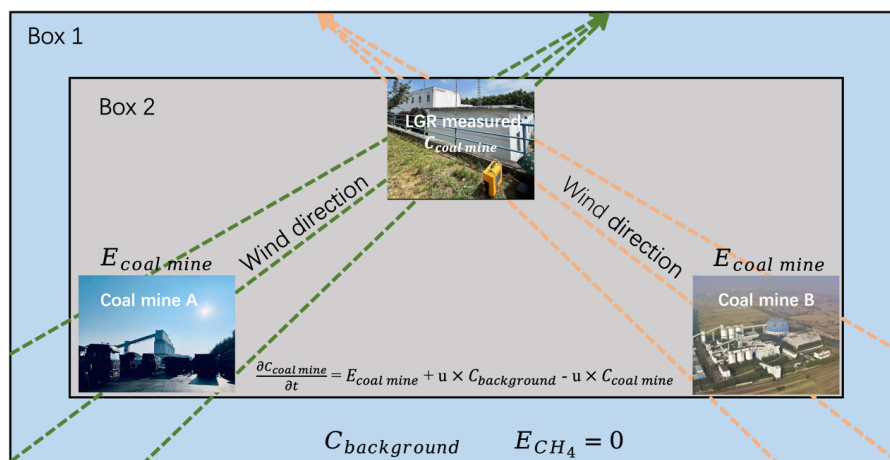
Figure 8. Schematic diagram of the 2-Box model.

2.7. Converting Emissions into Policy-Relevant Units

In order to compare the emissions with some other studies, the units (ppm min^{-1}) were converted into policy-relevant units (kg h^{-1}), although as outlined below, this conversion leads to a larger uncertainty range. According to the attribution analysis in Section 2.6, when the wind direction is located within a 60° arc of coal mine A or coal mine B (Figure 8), the respective CH$_4$ emissions which successfully passed attribution were assigned to the respective coal mine. Therefore, based on the wind direction, CH$_4$ emissions of coal mine A were screened from the CH$_4$ emissions captured at North 1km, and CH$_4$ emissions of coal mine B were screened from the CH$_4$ emissions captured at West 5km. adopting the following equation (7) to converte the units from ppm min^{-1} to kg h^{-1}:

$$E'_{CH_4} = E_{CH_4} \times \rho_{air} \times H \times A \times 60 \quad (7)$$

$$\rho_{air} = \frac{P \times M_{air}}{R \times T} \quad (8)$$

where E'_{CH_4} is the CH$_4$ emissions (kg h^{-1}), E_{CH_4} is the CH$_4$ emissions (ppm min^{-1}), ρ_{air} is the dry gas density (kg m^3) (based on equation 8), H is the height of the vertical rise that the emissions undergo within their first minute (m), A is the area (m^2) swept over an arc, which ranges linearly from 60° under slow wind conditions to 30° over very fast wind conditions, based on the wind speed when the direction is found to lead to successful attribution, P is the atmosphere pressure (Pa) over the sampling duration, M$_{air}$ is the molecular weight of dry air, which is a fixed constant (28.97×10^{-3} kg mol^{-1}), R is the universal gas constant (8.314J mol^{-1} k^{-1}), T is the air temperature (K) over the sampling duration.

Two different assumptions are made for the vertical extent of the plume rise, since the emissions are computed minute-by-minute which is shorter than the adjustment time throughout the entire boundary layer (Vaughn et al., 2018; Zinchenko et al., 2002). The first is to assume it has mixed within the bottom one fourth of the boundary layer, and the second is that it has mixed based on a steady vertical rise equal to one tenth of the horizontal wind. In this work, results using both assumptions will be presented.

3. Results and Discussion

11

3.1 Spatial Distribution Characteristics of CH$_4$ Concentration Around Coal Mine

Time series of CH$_4$ concentration, wind speed, and direction at 1 km, 3 km and 5 km north of CM-A are given in Figure 9a and Figure 9b. The wind direction blew from CM-A towards the observations (between 150° and 210°) 59.2% of the time, with only one day observed at 1km north (August 15) with a significant amount of wind from the west (between 240° and 300°) 92.8% of the time. Consistent with CM-A being the major source at 1km, when the wind blew from the south, the CH$_4$ concentration (3.45±0.79 ppm) was both higher and had a larger variation than when the wind blew from the west (2.40±0.17 ppm) which was similar to background conditions. This is consistent with there being no known significant sources to the west from this observation location, as shown in Figure 2. Similarly, under faster than average wind conditions from the direction of CM-A (on August 21 the mean wind was 5.70 m s^{-1} with 14.9% of observations faster than 7 m s^{-1}), the observed concentrations were slightly lower, yet similarly variable (3.17±0.82 ppm). All of these findings are consistent with transport dominating the concentrations at 1 km north, and that high frequency wind and concentration observations are required in tandem to compute the required spatial gradients in the CH$_4$, otherwise there is no basis to objectively separate the effects of the emitting region (CM-A) from the background.
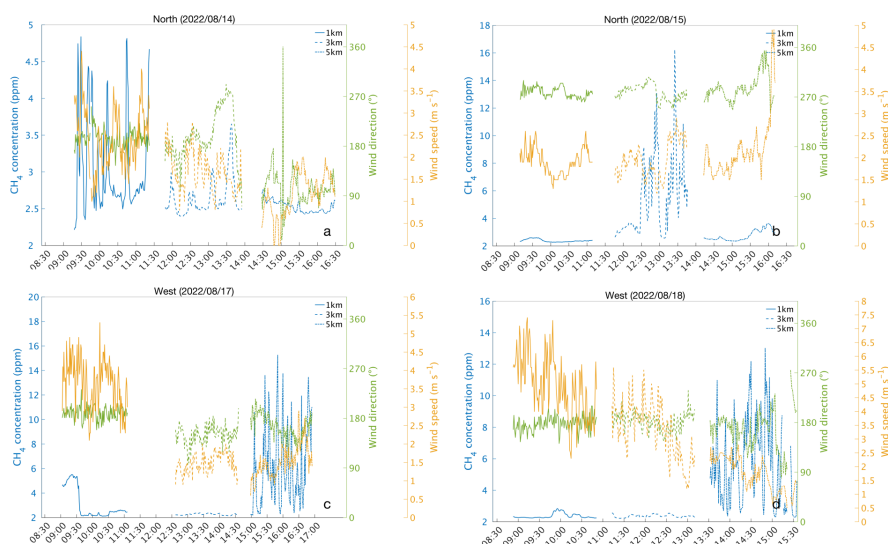
Figure 9. Time series of CH$_4$ concentration (ppm) (blue), wind speed (m s^{-1}) (yellow) and wind direction (º) (orange lines) measured at 1 km (solid), 3km (dashed) and 5km (dash-dot) located north (top) and west (bottom) of CM-A on four different days.

A similar set of findings were observed at 3 km north, while 5 km north is generally similar to the

267 background. At 3 km north, when the wind was from the south (59.3% of data), the concentration was

268 lower and more variable (3.16±1.48 ppm, with 78.7% of observations below 3.0 ppm) than at 1 km north,

269 consistent with advection from CM-A and a relatively stable atmosphere with a small contribution from

270 diffusion between the plume and the background. When the wind blew from other directions, the

271 distribution of concentrations broadened considerably, with a range from background (2.25 ppm) through

272 extremely polluted (16.2 ppm). One subset of this was observed on August 15 (observed over a total of

273 61 mins of observations, 6.68% of the total observations at 3 km north) when the wind was from the west

274 and slow, where the concentration was (5.44±2.82 ppm), as depicted in Figure 9. The data on this day

275 aligned with the presence of a major highway west of the observation site, which was observed in-person

276 to have heavy traffic consisting of vehicles carrying coal (which could still be outgassing) as well as

277 others powered by compressed natural gas (CNG). At 5km north the overall concentration (2.40±0.28

278 ppm) was generally lower than at 3km and had much lower variability, consistent with background CH_4.

279 Time series of CH_4 measured at 1 km, 3 km and 5 km west of CM-A and corresponding wind

280 direction and speed are given in Figure 9c and Figure 9d. Overall, the main wind direction is from the

281 south 98.4% of the time at 1km, 74.5% of the time at 3km, and 70.2% of the time at 5 km, and the wind

282 speed was very high when measuring CH_4 at 1 km west, with an average value of 4.28±1.13 m s^{-1} and a

283 maximum of 7.4 m s^{-1}. This set of findings is consistent with clean upwind sources. Accordingly at 1km

284 west, the observed CH_4 concentration was slightly higher than background and had similar variability to

285 1km and 3km north (2.71±0.94 ppm and 86.5% of the data below 3 ppm). At 3 km west, CH_4 was

286 observed to be similar to the background (2.32±0.09 ppm). The only exception was found at 1 km west

287 between 9:00 am and 9:30 am on August 17, in which all of the observations were greater than 4 ppm.

288 Since the areas to the west from 1 km west contains mostly farmland, there was no expected strong source

289 of CH_4, as shown in Figure 2. This indicates that during this special short time, the observed slow increase

290 and rapid fall-off in CH_4 concentration must be due an unidentified source, or a change in the boundary

291 layer or vertical mixing structure.

292 Following this, it was anticipated that the 5 km west site would exhibit background types of

293 conditions, however the observed data deviates significantly. Wind speed was low (1.63±0.54 m s^{-1},

294 maximum 3.0 m s^{-1}), CH_4 concentration was both very high and exhibited substantial temporal

295 variability (5.83±2.99 ppm, 66.7% exceeding 4 ppm, and peak of 15.3 ppm), and 70.2% of the

296 observations were from the south as demonstrated in Figure 10d,e,f. From Figure 1, it can be seen that

13

297   there is another coal mine (CM-B) located about 1 km away from the 5 km west measurement point, to

298   its southwest, although CM-B has an annual production of about 3 million tons (smaller than CM-A) and

299   not considered to be high gas (like CM-A), and therefore was not previously considered important. The

300   overlap of high concentrations with low a priori emissions, suggests that formal attribution is essential

301   to quantitatively confirm whether CM-B is the source responsible for both typical conditions at 5 km

302   west, as well as the long-range transport event at 1 km west.

303   CH_4 concentrations and wind observations in all directions except to the west, and except for the

304   small number of special events documents above, exhibit PDFs that show there is a decrease in

305   concentration the further the distance from CM-A (Figures 10 and 11), indicating that CM-A is consistent

306   with the major sources in these regions. These decreases are observed in terms of the median, mean,

307   distribution width, and percentage over 4.0 ppm all decreasing from 1 km north to 3 km north and again

308   from 3 km north to 5 km north.

309
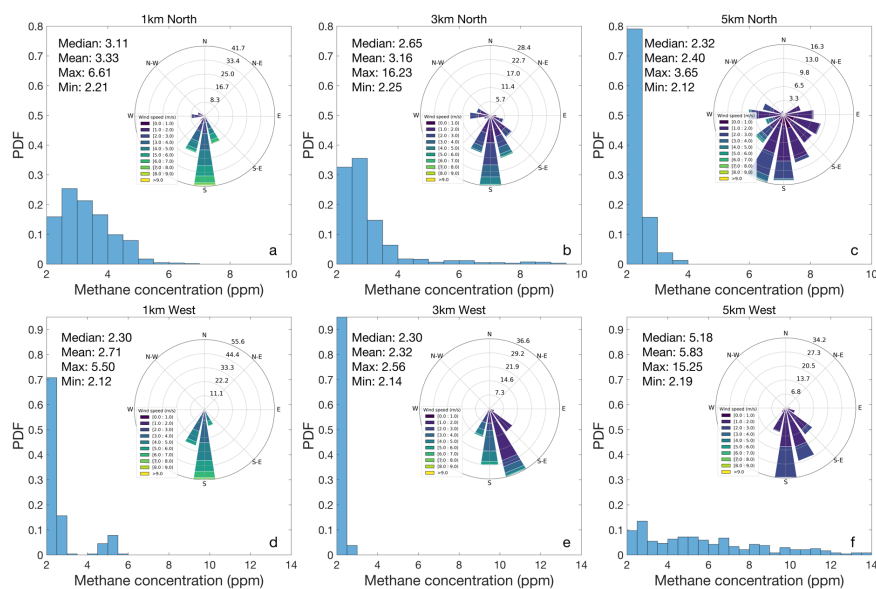
Figure 10. Probability density map for CH_4 concentration and wind rose measured at 1 km north (top left), 1 km west (bottom left), 3 km north (top center), 3 km west (bottom center), 5 km north (top right), and 5 km west (bottom right) of CM-A.
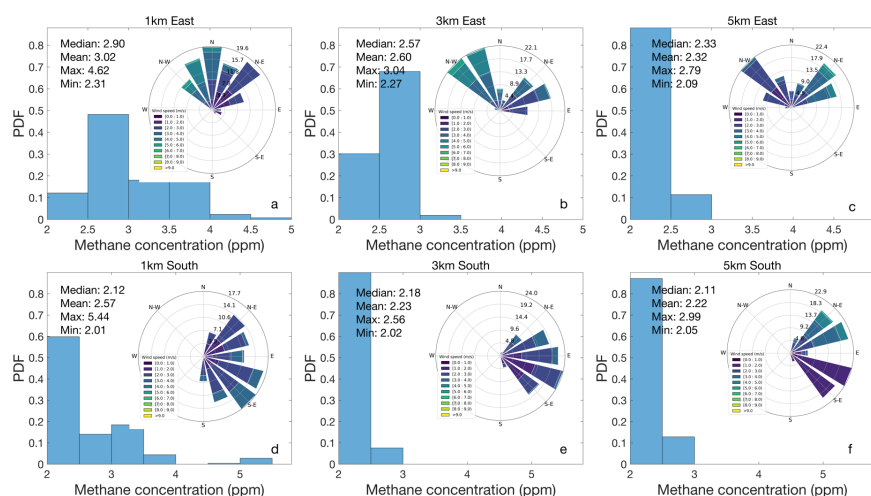
Figure 11. Probability density map for CH$_4$ concentration measured at 1 km, 3 km and 5 km east and south of CM-A and corresponding wind rose chart.

The observed CH$_4$ concentration gradient as one moves westward from CM-A is inconsistent with the other ordinal directions (Figure 10d, e, f). While there was a small decrease in the mean and distribution breadth from 1 km west to 3 km west, there was a large increase in the median, mean, distribution width, percentatge over 4.0 ppm from 3 km west to 5 km west. Furthermore, the data at 5 km west was found to be skewed differently than at the other sites, with approximately 70% of the data greater than 4.0 ppm. The data clearly indicates that the 5 km west site behaves more like a source region than even the 1 km north site.

3.2 Quantification and Emission Characteristics of CMM

The CH$_4$ emissions have been computed at each of the observation poits, with 25.7% of observations yielding emissions results. The PDFs of the CH$_4$ emissions (Figures 12 and 13) reveal that the three stations in the north and the 5km west station all are relatively high and variable, while the remainder are relatively low and non-variable. Among all the CH$_4$ emissions results, the highest median, mean, maximum, and breadth of the distribution are all observed at 5km west. The 3km south location has the lowest emissions of all points observed (by median), with a respective median, mean, maximum, and percentage greater than 1.0ppm/min of (0.03 ppm min^{-1}, 0.26 ppm min^{-1}, 0.90 ppm min^{-1}, 0%) (Figure 13), and is subsequently considered representative of background emissions in this work. It is important to note that there is no area within this region that has 0ppm/min emissions and that the minimum concentration on average is about 2.23 ppm (Figure 11), both of which are considered very high or

334   polluted compared with most other current studies (Irakulis-Loitxate et al., 2021; Sadavarte et al., 2021).

335
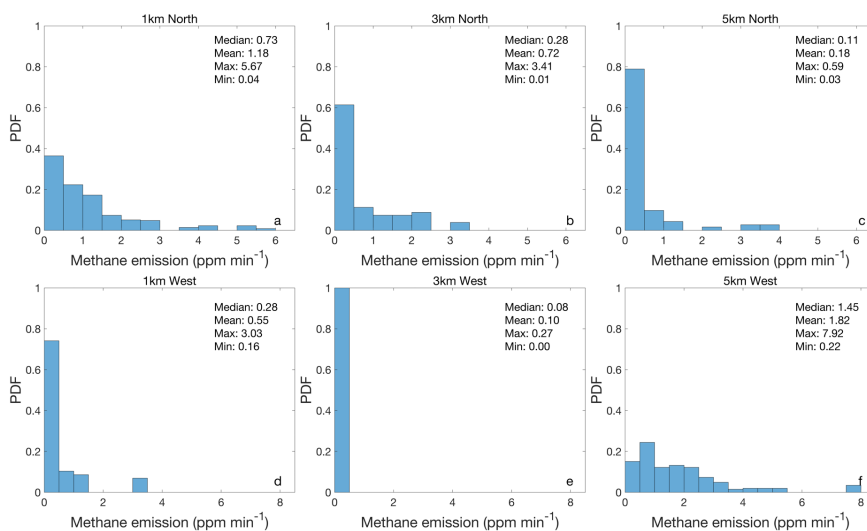
Figure 12. Probability density functions (PDF) of computed CH₄ emissions located at 1 km north (a), 3 km north (b), 5 km north (c), 1 km west (d), 3 km west (e), and 5 km west (f) of CM-A, including median, mean, maximum, and minimum statistics.

339
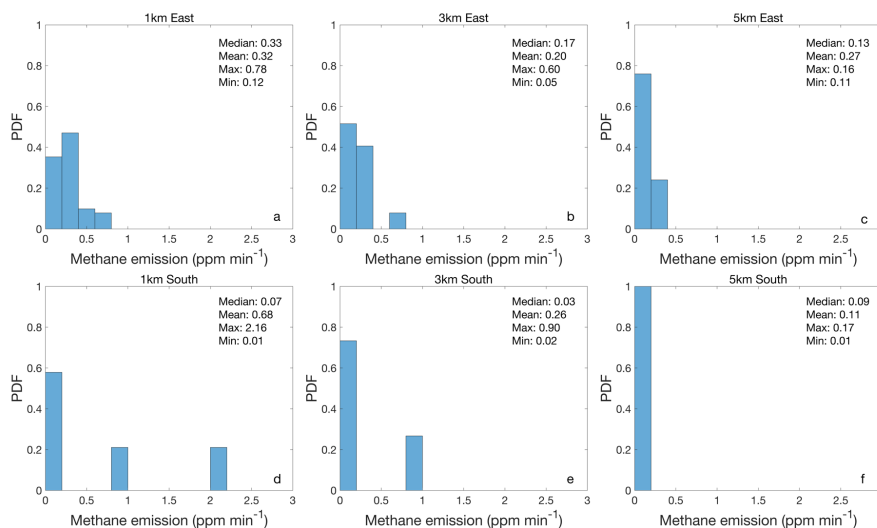
Figure 13. Probability density functions (PDF) of computed CH₄ emissions located at 1 km east (a), 3 km east (b), 5 km east (c), 1 km south (d), 3 km south (e), and 5 km south (f) of CM-A, including median, mean, maximum, and minimum statistics.

343   The spatial distribution Characteristics of the CH₄ emissions is similar to that of the CH₄

344   concentration observations (Figure 12). First, there is a decrease as one moves northward along the axis

345   away from CM-A, with the median, mean, maximum, and percentage of emissions greater than 1.0 ppm

346   min^{-1} at 1 km north (0.73 ppm min^{-1}, 1.18 ppm min^{-1}, 5.67 ppm min^{-1}, and 42%) all larger than at 3km

347   north (0.28 ppm min^{-1}, 0.72 ppm min^{-1}, 3.41 ppm min^{-1}, and 29%). The values at 3 km north are also

348   larger than those at 5 km north, which respectively are 0.11 ppm min^{-1}, 0.18 ppm min^{-1}, and 0.59 ppm

349   min^{-1}, and 0%. The subset of emissions under low wind speed conditions exhibited a larger decline from

350   1 km to 3 km and from 3 km to 5 km. The observations are further consistent with transport from a single

351   dominant source located at CM-A being the primary driving factor, and diffusion from other industrial

352   sources in Changzhi city center being a secondary factor.

353   Consistent with there being few to no sources impacting the 1 km west and 3 km west sites, except

354   for considerably less transport from CM-A the computed PDFs at these sites (Figure 12) demonstrate

355   low emissions and low variability, with the respective median, mean, maximum, and percentage of

356   emissions greater than 1.0 ppm min^{-1} at 1 km west being   0.28 ppm min^{-1}, 0.55 ppm min^{-1} , 3.03 ppm

357   min^{-1}, and 16% and at 3km west being even lower (0.08 ppm min^{-1}, 0.10 ppm min^{-1}, 0.27 ppm min^{-1}, and

358   0%). However, the CH_4 emissions computed at 5 km west were the highest and most variable of all results

359   computed in this work, with the respective statistics being 1.45 ppm min^{-1}, 1.82 ppm min^{-1}, 7.92 ppm

360   min^{-1}, and 60%. Furthermore, the skewness of the distribution at 5 km west (which has 30% of the CH_4

361   emissions above 2.0 ppm min^{-1}) is much larger than at 1 km north (which only has 15% of emissions

362   above 2.0 ppm min^{-1}). Combining these pieces of information, at first look it seems that the site at 5 km

363   west is not related to the emissions from CM-A, or at best are a mixture of emissions from CM-A and

364   those at another site, herein proposed to be CM-B. The remainder of this study focuses on disentangling

365   and attributing contributions from CM-A and CM-B at 5km west, with the observations at the remaining

366   sites ruled out in terms of having a contribution from CM-B.

367   **3.3 Attribution of CH_4 Emissions**

368   This works applied the 2-box model at the 5 km west site and quantified the contribution of both

369   CM-A and CM-B emissions to the observed CH_4 concentration distributions as given in Figure 14. First,

370   the results of the 2-box model produce PDFs which overlap with the overall observed CH_4 PDF,

371   indicating that the results are reasonable. Second, space of the emissions computed from the two different

372   two coal mines do not overlap, and cover two independent portions of the observed CH_4 PDF. Specifically,

373   the 30%, 50%, and 70% values of CH_4 concentration observed at 5km west are 3.68 ppm, 5.18 ppm, and

374   6.86 ppm respectively.   The emissions from CM-A yield a CH_4 concentration less than 4 ppm most of

375   the time, with a 30%, 50%, 70%, and maximum concentration of 2.96 ppm, 3.15 ppm, 3.31 ppm, and

376   4.60 ppm, while the emissions from CM-B yield a CH_4 concentration more than 5 ppm most of the time,

377   with a minimum, 30%, 50%, 70%, and maximum concentration of 4.76 ppm, 5.20 ppm, 5.68 ppm, and

378   6.18 ppm.

379   Overall, the emissions from CM-B cover well the observed concentration values from the range of

380   50% to 70%, with a single high value around the 90% value, while the emissions from CM-A cover well

381   the observed concentration values in the range from 10% to 30%. One weakness is that the length of

382   observations is not as comprehensive as at the other sites, and therefore it is possible that had more

383   observations been made, the contributions from CM-B would have filled more of the space between the

384   70% and 90% levels, and some combination of sources from CM-A and CM-B would have better filled

385   the space between the 30% and 50% levels. The results indicate to a high degree of certainty that the

386   emissions from the two respective coal mines are distinct, with CM-A the source of emissions in the

387   lower range of the concentration distribution and CM-B the source for emissions in the higher

388   concentration range, covering values in the middle and upper range. Improvements in modeling,

389   additional observations, considering possible contributions from additional missing sources, and

390   consideration of longer-range transport could add further improvement and better explore the

391   intermediate range of observed concentrations.
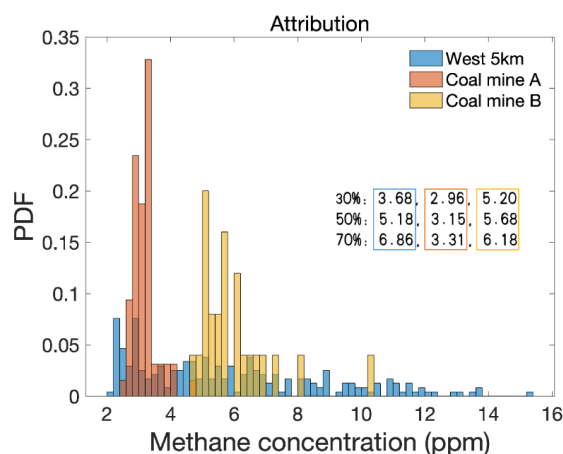
392

393   **Figure 14. The PDFs of CH_4 concentration measured at 5 km west (blue) and simulated using the 2-Box model**

394   **under conditions when the source is CM-A (red), and when the sources is CM-B (orange), including**

395   **representative 30%, 50%, and 70% bounds are in.**

396   **3.4 Policy-Relevant Emissions**

397   In order to compare the values of CH_4 emissions from the Shanxi coal mines computed in section

398   2.7, the units (ppm min^{-1}) are transformed into units of (kg h^{-1}) via a conversion factor based on equations

399   (7) and (8). This conversion increases the overall uncertainty, since since it involves approximations of

400   the area swept, the boundary layer height, and and other uncertainties. In this study, average CH$_4$

401   emissions from CM-A and CM-B are 13670±7400 kg h^{-1} and 5070±2270 kg h^{-1}, and the CH$_4$ emissions

402   range is from 200 kg hr^{-1} to 67700 kg hr^{-1} and 430 kg hr^{-1} to 15300 kg hr^{-1} repectivily (Table 2). Both mines

403   display a fat tail distribution, with respective 25th, median, and 75th percentile values of [870, 7500, 38700]

404   kg h^{-1} and [431, 1590, 7000] kg h^{-1}. respectively. These findings are demonstrated to be higher than CH$_4$

405   emissions from equivalent oil and gas operations in the USA (Chen et al., 2022), with one site being

406   roughly double and the other similar to and slightly lower than day-to-day emissions inverted over 5-

407   years from TROPOMI (Hu et al., 2024) over the same region. This is consistent with the fact that the

408   results herein target very high frequency and spatially confined emissions, while satellites provide day-

409   to-day values over a larger pixel area, as well as associated significant uncertainties involved in

410   converting from ppm to kg. In specific, at CM-A, the minimum (200 kg h^{-1}) and maxmum (67700 kg h$^-$

411   ^{1}) values of CH$_4$ emissions results are larger than the respective minimum (8 kg h^{-1}) and maxmum (37300

412   kg h^{-1}) values of CH$_4$ emissions inverted from TROPOMI, with the statistical values roughly double,

413   while at CM-B, the minimum (430 kg h^{-1}) value of CH$_4$ emissions results is greater than the minimum

414   (20 kg h^{-1}) from TROPOMI, the maxmum value (15300 kg h^{-1}) of CH$_4$ emissions is less than the

415   maximum (37300 kg h^{-1}) from TROPOMI, and the statistical values are slightly smaller although similar.

416   In this study, observations were made within 1km of the coal mines on a minute-to-minute basis, while

417   the the TROPOMI observed the xCH$_4$ over a space scale (5.5×7 km^2) and on a day-to-day average basis,

418   both of which indicate advantages of higher sampling diversity, especially so at the extreme values

419   observed, when compared with TROPOMI's results. For this reason, it is likely that the sampling time at

420   CM-B was insufficient to fully capture the fat tail of the emissions, since the maxmum is smaller than

421   the maximum estimated CH$_4$ from TROPOMI (consistent with the limited two days of data at coal mine

422   B), (Table 1). Given that the emissions are generally larger at the higher production coal mine, they are

423   consistent with the concept that over geologically similar environments, higher coal mine production

424   leads to increased CH$_4$ emissions, although the increase is not linear as most current models assume.

425

426

427

428

429

430

431

432 **Table 2. The CH$_4$ emissions (kg h^{-1}) of CM-A and CM-B using different observation methods and statistical**

433 **methods**

Coal mines	High frequency ground observation CH$_4$ emissions (kg h^{-1})								TROPOMI inverted CH$_4$ emissions (kg h^{-1})			
	1/4 boundary layer				1/10 horizontal wind							
	Mean±SE	Min	Median	Max	Mean±SE	Min	Median	Max	Mean±SE	Min	Median	Max
CM-A	13670±7400	200	7500	67700	19100±9800	70	5790	63800	5500±700	8	2130	24900
CM-B	5070±2270	430	6060	15300	1000±444	30	1600	2850	6200±1000	20	1450	37300

434 **4. Conclusions**

435   This study presents a high frequency ground observation campaign and a new analytical top down

436   emissions estimation approach to quantify the emissions of CH$_4$ from a high gas coal mine region with

437   multiple mines. The base observations are made using a portable greenhouse gas analyzer in connection

438   with meterological and other optical measurements. Observations have been made over 15 days at a

439   frequency of 1 second, at various locations of known distance from an existing high production coal

440   mine. The high frequency observations are then used in connection with a mass conserving modeling

441   platform to estimate the CH$_4$ emission rate. A mass-conserving Two-Box model was used for attribution

442   analysis in this study. The results show that the spatial characteristics of CH$_4$ concentration/emissions are

443   consistent with the distance from a well characterized of single coal mine within 5km distance, and CH$_4$

444   emissions demonstrate clear first order effects of both transport and diffusion, with methane emission

445   rates of 0.73, 0.28 and 0.15 ppm min^{-1} at 1, 3 and 5 km downwind respectively. At 5 km north the overall

446   concentration (2.40±0.28 ppm) was generally lower than at 3km and had much lower variability,

447   consistent with background CH$_4$, which demonstrate that the CMM emissions mainl affect the

448   surrounding area with 5km distance. However, the overlap of two coal mines (CM-A and CM-B) have a

449   far more complex distribution of emissions intensity, ranging as high as 1.82 ppm min^{-1}, which is much

450   higher than the emissions of single source at any directions. Another, the background concentration of

451   surface CH$_4$ in the mining areas is very high compared with other studies, with a value always at and

452   above 2.23 ppm. Finally, in order to compare these results with results from other parts of the world, the

453   subset of emissions which successfully underwent attribution were converted into the unit of kg h^{-1} using

454   an approximation of the volume swept by the wind and other approximations of the atmosphere. The

455   resulting values were found to be 13670±7400 kg h^{-1} and 5070±2270 kg h^{-1} respectively, which are higher

456   than CH_4 emissions from equivalent oil and gas operations in the USA, and in one case are higher than

457   but in the other case similar to day-to-day emissions inverted from 5-years of TROPOMI over the same

458   region.

459   This work demonstrates that high frequency surface observations of CH_4, in combination with high

460   frequency observations of wind can provide deep insights into emissions by accounting for high

461   frequency changes in space and time at the same time, which tend to be missing from models which used

462   more idealized approaches (such as average plume shapes and sizes, levels of coal production, and

463   interpreting gradients from a small number of fixed images). A significant source of CH_4 emissions from

464   a previously unknown or improperly classified mine may pose a vastly different range of observed

465   concentration as well as computed emissions than expected. The importance of observations at both high

466   frequency and regional spatial coverage are demonstrated, and a set of practical methods that are freely

467   open and can be adopted and modified rapidly are provided. The approach to source attribution used

468   herein can provide insights to policymakers to formulate regional emission control policies and provide

469   a check on or a priori assumption for the new generation of advance satellite-based top-down emissions

470   estimates, while demonstrating that spatial attribution is a critical next-step for satellite approximations

471   and CH_4 control policies.

472   **Data Availability**

473   All underlying data herein are available for access by the editors and reviewers at

474   https://figshare.com/s/1a393772d7b72ae17e62 and will be made available to the community upon

475   publication.

476   **Author contributions**

477   K.Q., J.B.C. and F.L. designed the research; F.L., C.Y., and Y.S. collected the data; J.B.C. and F.L.

478   analyzed the data; Q.T., W. H. and Q.X. provided the support for data analysis and drawing; Q.H., S.W

479   gave suggestion on running the 2-Box model; F.L. wrote the manuscript with inputs from J.B.C., Q.H.

480   and P.T.; All authors discussed the results and contributed to the final manuscript.

481   **Competing interests**

482   The authors declare that they have no known competing financial interests or personal relationships that

483   could have appeared to influence the work reported in this paper.

484   **Disclaimer**

485   Publisher's note: Copernicus Publications remains neutral with regard to jurisdictional claims made in

486 the text, pub- lished maps, institutional affiliations, or any other geographical rep- resentation in this

487 paper. While Copernicus Publications makes ev- ery effort to include appropriate place names, the final

488 responsibility lies with the authors.

489 **Acknowledgments**

495

496 **References**

497 Allen, D. T.: Methane emissions from natural gas production and use: reconciling bottom-up and top-

498 down measurements, Curr. Opin. Chem., 5, 78-83, https://doi.org/10.1016/j.coche.2014.05.004, 2014.

499 Bloom, A. A., Bowman, K. W., Lee, M., Turner, A. J., Schroeder, R., Worden, J. R., Weidner, R.,

500 McDonald, K. C., and Jacob, D. J.: A global wetland methane emissions and uncertainty dataset for

501 atmospheric chemical transport models (WetCHARTs version 1.0), Geosci. Model Dev., 10, 2141-2156,

502 https://gmd.copernicus.org/articles/10/2141/2017/, 2017.

503 Bournazian, J.: US. Energy Information Administration, https://hdl.handle.net/1813/4504, 2016.

504 Brandt, A. R., Heath, G. A., Kort, E. A., O'Sullivan, F., Pétron, G., Jordaan, S. M., Tans, P., Wilcox, J.,

505 Gopstein, A. M., Arent, D., Wofsy, S., Brown, N. J., Bradley, R., Stucky, G. D., Eardley, D., and Harriss,

506 R.: Methane Leaks from North American Natural Gas Systems, Science, 343, 733-735,

507 https://www.science.org/doi/abs/10.1126/science.1247045, 2014.

508 Brasseur, G. P., and Jacob, D. J.: Modeling of atmospheric chemistry, Cambridge University

509 Press Publishing, 2017.

510 Buchwitz, M., Schneising, O., Reuter, M., Heymann, J., Krautwurst, S., Bovensmann, H., Burrows, J. P.,

511 Boesch, H., Parker, R. J., Somkuti, P., Detmers, R. G., Hasekamp, O. P., Aben, I., Butz, A., Frankenberg,

512 C., and Turner, A. J.: Satellite-derived methane hotspot emission estimates using a fast data-driven

513 method, Atmos. Chem. Phys., 17, 5751-5774, https://acp.copernicus.org/articles/17/5751/2017/, 2017.

514 Butz, A., Galli, A., Hasekamp, O., Landgraf, J., Tol, P., and Aben, I.: TROPOMI aboard Sentinel-5

515 Precursor: Prospective performance of CH_4 retrievals for aerosol and cirrus loaded atmospheres, Remote

516   Sens. Environ., 120, 267-276, https://doi.org/10.1016/j.rse.2011.05.030, 2012.

517   Cao, X.: Policy and regulatory responses to coalmine closure and coal resources consolidation for

518   sustainability in Shanxi, China, J. Clean. Prod., 145, 199-208,

519   https://doi.org/10.1016/j.jclepro.2017.01.050, 2017.

520   Chen, Y., Sherwin, E. D., Berman, E. S. F., Jones, B. B., Gordon, M. P., Wetherley, E. B., Kort, E. A.,

521   and Brandt, A. R.: Quantifying Regional Methane Emissions in the New Mexico Permian Basin with a

522   Comprehensive Aerial Survey, Environ. Sci. Technol., 56, 4317-4323,

523   https://doi.org/10.1021/acs.est.1c06458, 2022.

524   Cohen, J. B., and Prinn, R. G.: Development of a fast, urban chemistry metamodel for inclusion in global

525   models, Atmos. Chem. Phys., 11, 7629-7656, https://acp.copernicus.org/articles/11/7629/2011/, 2011.

526   Cohen, J. B., and Wang, C.: Estimating global black carbon emissions using a top-down Kalman Filter

527   approach, J. Geophys Res: Atmos., 119, 307-323, https://doi.org/10.1002/2013JD019912, 2014.

528   Delkash, M., Zhou, B., Han, B., Chow, F. K., Rella, C. W., and Imhoff, P. T.: Short-term landfill methane

529   emissions dependency on wind, Waste Management, 55, 288-298,

530   https://doi.org/10.1016/j.wasman.2016.02.009, 2016.

531   Duren, R. M., Thorpe, A. K., Foster, K. T., Rafiq, T., Hopkins, F. M., Yadav, V., Bue, B. D., Thompson,

532   D. R., Conley, S., Colombi, N. K., Frankenberg, C., McCubbin, I. B., Eastwood, M. L., Falk, M., Herner,

533   J. D., Croes, B. E., Green, R. O., and Miller, C. E.: California's methane super-emitters, Nature, 575,

534   180-184, https://doi.org/10.1038/s41586-019-1720-3, 2019.

535   Etminan, M., Myhre, G., Highwood, E. J., and Shine, K. P.: Radiative forcing of carbon dioxide, methane,

536   and nitrous oxide: A significant revision of the methane radiative forcing, Geophys. Res. Lett., 43, 12614-

537   12623, https://doi.org/10.1002/2016GL071930, 2016.

538   Goldsmith, C. D., Chanton, J., Abichou, T., Swan, N., Green, R., and Hater, G.: Methane emissions from

539   20 landfills across the United States using vertical radial plume mapping, J. Air Waste Manage., 62, 183-

540   197, https://doi.org/10.1080/10473289.2011.639480, 2012.

541   Gorchov Negron, A. M., Kort, E. A., Conley, S. A., and Smith, M. L.: Airborne Assessment of Methane

542   Emissions from Offshore Platforms in the U.S. Gulf of Mexico, Environ. Sci.Technol., 54, 5112-5120,

543   https://doi.org/10.1021/acs.est.0c00179, 2020.

544   Heerah, S., Frausto-Vicencio, I., Jeong, S., Marklein, A. R., Ding, Y., Meyer, A. G., Parker, H. A., Fischer,

545   M. L., Franklin, J. E., Hopkins, F. M., and Dubey, M.: Dairy Methane Emissions in California's San

23

546 Joaquin Valley Inferred With Ground-Based Remote Sensing Observations in the Summer and Winter,

547 Journal of Geophys Res: Atmo., 126, e2021JD034785, https://doi.org/10.1029/2021JD034785, 2021.

548 Hiller, R. V., Neininger, B., Brunner, D., Gerbig, C., Bretscher, D., Künzle, T., Buchmann, N., and Eugster,

549 W.: Aircraft-based CH₄ flux estimates for validation of emissions from an agriculturally dominated area

550 in   Switzerland,   Journal   of   Geophys   Res: Atmos.,   119,   4874-4887,

551 https://doi.org/10.1002/2013JD020918, 2014.

552 Hu, H., Landgraf, J., Detmers, R., Borsdorff, T., Aan de Brugh, J., Aben, I., Butz, A., and Hasekamp, O.:

553 Toward Global Mapping of Methane With TROPOMI: First Results and Intersatellite Comparison to

554 GOSAT, Geophys. Res. Lett., 45, 3682-3689, https://doi.org/10.1002/2018GL077259, 2018.

555 Irakulis-Loitxate, I., Guanter, L., Liu, Y.-N., Varon, D. J., Maasakkers, J. D., Zhang, Y., Chulakadabba,

556 A., Wofsy, S. C., Thorpe, A. K., Duren, R. M., Frankenberg, C., Lyon, D. R., Hmiel, B., Cusworth, D.

557 H., Zhang, Y., Segl, K., Gorroño, J., Sánchez-García, E., Sulprizio, M. P., Cao, K., Zhu, H., Liang, J., Li,

558 X., Aben, I., and Jacob, D. J.: Satellite-based survey of extreme methane emissions in the Permian basin,

559 Sci. Adv., 7, eabf4507, https://www.science.org/doi/abs/10.1126/sciadv.abf4507, 2021.

560 Jacob, D. J., Turner, A. J., Maasakkers, J. D., Sheng, J., Sun, K., Liu, X., Chance, K., Aben, I., McKeever,

561 J., and Frankenberg, C.: Satellite observations of atmospheric methane and their value for quantifying

562 methane   emissions,   Atmos.   Chem.   Phys.,   16,   14371-14396,

563 https://acp.copernicus.org/articles/16/14371/2016/, 2016.

564 Jacob, D. J., Varon, D. J., Cusworth, D. H., Dennison, P. E., Frankenberg, C., Gautam, R., Guanter, L.,

565 Kelley, J., McKeever, J., Ott, L. E., Poulter, B., Qu, Z., Thorpe, A. K., Worden, J. R., and Duren, R. M.:

566 Quantifying methane emissions from the global scale down to point sources using satellite observations

567 of   atmospheric   methane,   Atmos.   Chem.   Phys.,   22,   9617-9646,

568 https://acp.copernicus.org/articles/22/9617/2022/, 2022.

569 Janssens-Maenhout, G., Crippa, M., Guizzardi, D., Muntean, M., and Petrescu, A. M. R.: EDGAR v4.3.2

570 Global Atlas of the three major Greenhouse Gas Emissions for the period 1970–2012, Earth Syst. Sci.

571 Data, 1-55, https://doi.org/10.5194/essd-2017-79, 2017.

572 Karion, A., Sweeney, C., Pétron, G., Frost, G., Michael Hardesty, R., Kofler, J., Miller, B. R., Newberger,

573 T., Wolter, S., Banta, R., Brewer, A., Dlugokencky, E., Lang, P., Montzka, S. A., Schnell, R., Tans, P.,

574 Trainer, M., Zamora, R., and Conley, S.: Methane emissions estimate from airborne measurements over

575 a   western   United   States   natural   gas   field,   Geophys.   Res.   Lett.,   40,   4393-4397,

576 https://doi.org/10.1002/grl.50811, 2013.

577 Katzenstein, A. S., Doezema, L. A., Simpson, I. J., Blake, D. R., and Rowland, F. S.: Extensive regional

578 atmospheric hydrocarbon pollution in the southwestern United States, PNAS, 100, 11975-11979,

579 https://www.pnas.org/doi/abs/10.1073/pnas.1635258100, 2003.

580 Kerr, T., and Yang, M.: Coal mine methane in China: A budding asset with the potential to bloom, IEA

581 Information Paper, 1-35, https://www.iea.org/reports/coal-mine-methane-in-china-a-budding-asset-

582 with-the-potential-to-bloom, 2009.

583 Kirschke, S., Bousquet, P., Ciais, P., Saunois, M., Canadell, J. G., Dlugokencky, E. J., Bergamaschi, P.,

584 Bergmann, D., Blake, D. R., Bruhwiler, L., Cameron-Smith, P., Castaldi, S., Chevallier, F., Feng, L.,

585 Fraser, A., Heimann, M., Hodson, E. L., Houweling, S., Josse, B., Fraser, P. J., Krummel, P. B., Lamarque,

586 J.-F., Langenfelds, R. L., Le Quéré, C., Naik, V., O'Doherty, S., Palmer, P. I., Pison, I., Plummer, D.,

587 Poulter, B., Prinn, R. G., Rigby, M., Ringeval, B., Santini, M., Schmidt, M., Shindell, D. T., Simpson, I.

588 J., Spahni, R., Steele, L. P., Strode, S. A., Sudo, K., Szopa, S., van der Werf, G. R., Voulgarakis, A., van

589 Weele, M., Weiss, R. F., Williams, J. E., and Zeng, G.: Three decades of global methane sources and

590 sinks, Nat. Geosci., 6, 813-823, https://doi.org/10.1038/ngeo1955, 2013.

591 Krautwurst, S., Gerilowski, K., Borchardt, J., Wildmann, N., Gałkowski, M., Swolkień, J., Marshall, J.,

592 Fiehn, A., Roiger, A., Ruhtz, T., Gerbig, C., Necki, J., Burrows, J. P., Fix, A., and Bovensmann, H.:

593 Quantification of CH_4 coal mining emissions in Upper Silesia by passive airborne remote sensing

594 observations with the Methane Airborne MAPper (MAMAP) instrument during the CO_2 and Methane

595 (CoMet) campaign, Atmos. Chem. Phys., 21, 17345-17371,

596 https://acp.copernicus.org/articles/21/17345/2021/, 2021.

597 Krautwurst, S., Gerilowski, K., Jonsson, H. H., Thompson, D. R., Kolyer, R. W., Iraci, L. T., Thorpe, A.

598 K., Horstjann, M., Eastwood, M., Leifer, I., Vigil, S. A., Krings, T., Borchardt, J., Buchwitz, M.,

599 Fladeland, M. M., Burrows, J. P., and Bovensmann, H.: Methane emissions from a Californian landfill,

600 determined from airborne remote sensing and in situ measurements, Atmos. Meas. Tech., 10, 3429-3452,

601 https://amt.copernicus.org/articles/10/3429/2017/, 2017.

602 Kuhlmann, G., Brunner, D., Emmenegger, L., Schwietzke, S., Zavala-Araiza, D., Thorpe, A., Hueni, A.,

603 and Röckmann, T.: Quantifying methane super-emitters from oil and gas production in Romania with the

604 AVIRIS-NG imaging spectrometer, EGU General Assembly 2023, Vienna, Austria., 24–28 Apr 2023

605 EGU23-6751.

606   Kuze, A., Suto, H., Nakajima, M., and Hamazaki, T.: Thermal and near infrared sensor for carbon

607   observation Fourier-transform spectrometer on the Greenhouse Gases Observing Satellite for greenhouse

608   gases monitoring, Appl. Optics., 48, 6716-6733, https://opg.optica.org/ao/abstract.cfm?URI=ao-48-35-

609   6716, 2009.

610   Lauvaux, T., Giron, C., Mazzolini, M., d'Aspremont, A., Duren, R., Cusworth, D., Shindell, D., and Ciais,

611   P.: Global assessment of oil and gas methane ultra-emitters, Science, 375, 557-561,

612   https://www.science.org/doi/abs/10.1126/science.abj4351, 2022.

613   Li, Q., Fernandez, R. P., Hossaini, R., Iglesias-Suarez, F., Cuevas, C. A., Apel, E. C., Kinnison, D. E.,

614   Lamarque, J.-F., and Saiz-Lopez, A.: Reactive halogens increase the global methane lifetime and

615   radiative forcing in the 21st century, Nat. Commun., 13, 2768, https://doi.org/10.1038/s41467-022-

616   30456-8, 2022.

617   Li, X., Cohen, J. B., Qin, K., Geng, H., Wu, L., Wu, X., Yang, C., Zhang, R., and Zhang, L.: Remotely

618   Sensed and Surface Measurement Derived Mass-Conserving Inversion of Daily High-Resolution NOx

619   Emissions and Inferred Combustion Technologies in Energy Rich Northern China, Atmos. Chem. Phys.,

620   23, 8001-8019, https://egusphere.copernicus.org/preprints/2023/egusphere-2023-2/, 2023,.

621   Lin, B.-q., and Liu, J.-h.: Estimating coal production peak and trends of coal imports in China, Energ.

622   Policy, 38, 512-519, https://doi.org/10.1016/j.enpol.2009.09.042, 2010.

623   Luther, A., Kleinschek, R., Scheidweiler, L., Defratyka, S., Stanisavljevic, M., Forstmaier, A., Dandocsi,

624   A., Wolff, S., Dubravica, D., Wildmann, N., Kostinek, J., Jöckel, P., Nickl, A. L., Klausner, T., Hase, F.,

625   Frey, M., Chen, J., Dietrich, F., Nęcki, J., Swolkień, J., Fix, A., Roiger, A., and Butz, A.: Quantifying

626   CH_4 emissions from hard coal mines using mobile sun-viewing Fourier transform spectrometry, Atmos.

627   Meas. Tech., 12, 5217-5230, https://amt.copernicus.org/articles/12/5217/2019/, 2019.

628   Luther, A., Kostinek, J., Kleinschek, R., Defratyka, S., Stanisavljević, M., Forstmaier, A., Dandocsi, A.,

629   Scheidweiler, L., Dubravica, D., Wildmann, N., Hase, F., Frey, M. M., Chen, J., Dietrich, F., Nęcki, J.,

630   Swolkień, J., Knote, C., Vardag, S. N., Roiger, A., and Butz, A.: Observational constraints on methane

631   emissions from Polish coal mines using a ground-based remote sensing network, Atmos. Chem. Phys.,

632   22, 5859-5876, https://acp.copernicus.org/articles/22/5859/2022/, 2022.

633   Mehrotra, S., Faloona, I., Suard, M., Conley, S., and Fischer, M. L.: Airborne Methane Emission

634   Measurements for Selected Oil and Gas Facilities Across California, Environ. Sci. Technol., 51, 12981-

635   12987, https://doi.org/10.1021/acs.est.7b03254, 2017.

636 Miller, S. M., Michalak, A. M., Detmers, R. G., Hasekamp, O. P., Bruhwiler, L. M. P., and Schwietzke,

637 S.: China's coal mine methane regulations have not curbed growing emissions, Nat. Commun., 10, 303,

638 https://doi.org/10.1038/s41467-018-07891-7, 2019.

639 Molina, L. T., Madronich, S., Gaffney, J. S., Apel, E., de Foy, B., Fast, J., Ferrare, R., Herndon, S.,

640 Jimenez, J. L., Lamb, B., Osornio-Vargas, A. R., Russell, P., Schauer, J. J., Stevens, P. S., Volkamer, R.,

641 and Zavala, M.: An overview of the MILAGRO 2006 Campaign: Mexico City emissions and their

642 transport and transformation, Atmos. Chem. Phys., 10, 8697-8760,

643 https://acp.copernicus.org/articles/10/8697/2010/, 2010.

644 Peng, S., Piao, S., Bousquet, P., Ciais, P., Li, B., Lin, X., Tao, S., Wang, Z., Zhang, Y., and Zhou, F.:

645 Inventory of anthropogenic methane emissions in mainland China from 1980 to 2010, Atmos. Chem.

646 Phys., 16, 14545-14562, https://acp.copernicus.org/articles/16/14545/2016/, 2016.

647 Plant, G., Kort, E. A., Murray, L. T., Maasakkers, J. D., and Aben, I.: Evaluating urban methane emissions

648 from space using TROPOMI methane and carbon monoxide observations, Remote Sen. Environ., 268,

649 112756, https://doi.org/10.1016/j.rse.2021.112756, 2022.

650 Povey, A. C., and Grainger, R. G.: Known and unknown unknowns: uncertainty estimation in satellite

651 remote sensing, Atmos. Meas. Tech., 8, 4699-4718, https://amt.copernicus.org/articles/8/4699/2015/,

652 2015.

653 Prather, M. J., Holmes, C. D., and Hsu, J.: Reactive greenhouse gas scenarios: Systematic exploration of

654 uncertainties and the role of atmospheric chemistry, Geophys. Res. Lett., 39, L09803,

655 https://doi.org/10.1029/2012GL051440, 2012.

656 Prinn, R., Cunnold, D., Rasmussen, R., Simmonds, P., Alyea, F., Crawford, A., Fraser, P., and Rosen, R.:

657 Atmospheric Trends in Methylchloroform and the Global Average for the Hydroxyl Radical, Science,

658 238, 945-950, https://www.science.org/doi/abs/10.1126/science.238.4829.945, 1987.

659 Qin, K., Hu, W., He, Q., Lu, F., and Cohen, J. B.: Individual Coal Mine Methane Emissions Constrained

660 by Eddy-Covariance Measurements: Low Bias and Missing Sources, EGUsphere, 1-49,

661 https://egusphere.copernicus.org/preprints/2023/egusphere-2023-1210/, 2023a.

662 Qin, K., Lu, L., Liu, J., He, Q., Shi, J., Deng, W., Wang, S., and Cohen, J. B.: Model-free daily inversion

663 of NOx emissions using TROPOMI (MCMFE-NOx) and its uncertainty: Declining regulated emissions

664 and growth of new sources, Remote Sens. Environ., 295, 113720,

665 https://doi.org/10.1016/j.rse.2023.113720, 2023b.

666 Reuter, M., Buchwitz, M., Schneising, O., Krautwurst, S., O'Dell, C. W., Richter, A., Bovensmann, H.,

667 and Burrows, J. P.: Towards monitoring localized CO_2 emissions from space: co-located regional CO_2

668 and NO_2 enhancements observed by the OCO-2 and S5P satellites, Atmos. Chem. Phys., 19, 9371-9383,

669 https://acp.copernicus.org/articles/19/9371/2019/, 2019.

670 Rigby, M., Park, S., Saito, T., Western, L. M., Redington, A. L., Fang, X., Henne, S., Manning, A. J.,

671 Prinn, R. G., Dutton, G. S., Fraser, P. J., Ganesan, A. L., Hall, B. D., Harth, C. M., Kim, J., Kim, K. R.,

672 Krummel, P. B., Lee, T., Li, S., Liang, Q., Lunt, M. F., Montzka, S. A., Mühle, J., O'Doherty, S., Park,

673 M. K., Reimann, S., Salameh, P. K., Simmonds, P., Tunnicliffe, R. L., Weiss, R. F., Yokouchi, Y., and

674 Young, D.: Increase in CFC-11 emissions from eastern China based on atmospheric observations, Nature,

675 569, 546-550, https://doi.org/10.1038/s41586-019-1193-4, 2019.

676 Sadavarte, P., Pandey, S., Maasakkers, J. D., Lorente, A., Borsdorff, T., Denier van der Gon, H.,

677 Houweling, S., and Aben, I.: Methane Emissions from Superemitting Coal Mines in Australia Quantified

678 Using TROPOMI Satellite Observations, Environ. Sci. Technol., 55, 16573-16580,

679 https://doi.org/10.1021/acs.est.1c03976, 2021.

680 Saunois, M., Stavert, A. R., Poulter, B., Bousquet, P., Canadell, J. G., Jackson, R. B., Raymond, P. A.,

681 Dlugokencky, E. J., Houweling, S., Patra, P. K., Ciais, P., Arora, V. K., Bastviken, D., Bergamaschi, P.,

682 Blake, D. R., Brailsford, G., Bruhwiler, L., Carlson, K. M., Carrol, M., Castaldi, S., Chandra, N.,

683 Crevoisier, C., Crill, P. M., Covey, K., Curry, C. L., Etiope, G., Frankenberg, C., Gedney, N., Hegglin,

684 M. I., Höglund-Isaksson, L., Hugelius, G., Ishizawa, M., Ito, A., Janssens-Maenhout, G., Jensen, K. M.,

685 Joos, F., Kleinen, T., Krummel, P. B., Langenfelds, R. L., Laruelle, G. G., Liu, L., Machida, T., Maksyutov,

686 S., McDonald, K. C., McNorton, J., Miller, P. A., Melton, J. R., Morino, I., Müller, J., Murguia-Flores,

687 F., Naik, V., Niwa, Y., Noce, S., O'Doherty, S., Parker, R. J., Peng, C., Peng, S., Peters, G. P., Prigent, C.,

688 Prinn, R., Ramonet, M., Regnier, P., Riley, W. J., Rosentreter, J. A., Segers, A., Simpson, I. J., Shi, H.,

689 Smith, S. J., Steele, L. P., Thornton, B. F., Tian, H., Tohjima, Y., Tubiello, F. N., Tsuruta, A., Viovy, N.,

690 Voulgarakis, A., Weber, T. S., van Weele, M., van der Werf, G. R., Weiss, R. F., Worthy, D., Wunch, D.,

691 Yin, Y., Yoshida, Y., Zhang, W., Zhang, Z., Zhao, Y., Zheng, B., Zhu, Q., Zhu, Q., and Zhuang, Q.: The

692 Global Methane Budget 2000–2017, Earth Syst. Sci. Data, 12, 1561-1623,

693 https://essd.copernicus.org/articles/12/1561/2020/, 2020a.

694 Saunois, M., Stavert, A. R., Poulter, B., Bousquet, P., and Zhuang, Q.: The Global Methane Budget 2000–

695 2017, Earth System Science Data, 12, 1561-1623, https://doi.org/10.5194/essd-12-1561-2020, 2020b.

696   Shi, T., Han, G., Ma, X., Mao, H., Chen, C., Han, Z., Pei, Z., Zhang, H., Li, S., and Gong, W.: Quantifying

697   factory-scale CO_2/CH_4 emission based on mobile measurements and EMISSION-PARTITION model:

698   cases in China, Environ. Res. Lett., 18, 034028, https://dx.doi.org/10.1088/1748-9326/acbce7, 2023.

699   Shi, T., Han, Z., Han, G., Ma, X., Chen, H., Andersen, T., Mao, H., Chen, C., Zhang, H., and Gong, W.:

700   Retrieving CH4-emission rates from coal mine ventilation shafts using UAV-based AirCore observations

701   and the genetic algorithm–interior point penalty function (GA-IPPF) model, Atmos. Chem. Phys., 2,

702   13881-13896, https://acp.copernicus.org/articles/22/13881/2022/, 2022.

703   Sun, K.: Derivation of Emissions From Satellite-Observed Column Amounts and Its Application to

704   TROPOMI NO_2 and CO Observations, Geophys. Res. Lett. , 49, e2022GL101102,

705   https://doi.org/10.1029/2022GL101102, 2022.

706   Tong, X., van Heuven, S., Scheeren, B., Kers, B., Hutjes, R., and Chen, H.: Aircraft-Based AirCore

707   Sampling for Estimates of N_2O and CH_4 Emissions, Environ. Sci. Technol., 57, 15571-15579,

708   https://doi.org/10.1021/acs.est.3c04932, 2023.

709   Tu, Q., Hase, F., Schneider, M., García, O., Blumenstock, T., Borsdorff, T., Frey, M., Khosrawi, F.,

710   Lorente, A., Alberti, C., Bustos, J. J., Butz, A., Carreño, V., Cuevas, E., Curcoll, R., Diekmann, C. J.,

711   Dubravica, D., Ertl, B., Estruch, C., León-Luis, S. F., Marrero, C., Morgui, J. A., Ramos, R., Scharun, C.,

712   Schneider, C., Sepúlveda, E., Toledano, C., and Torres, C.: Quantification of CH_4 emissions from waste

713   disposal sites near the city of Madrid using ground- and space-based observations of COCCON,

714   TROPOMI and IASI, Atmos. Chem. Phys., 22, 295-317, https://acp.copernicus.org/articles/22/295/2022/,

715   2022.

716   Varon, D. J., Jacob, D. J., McKeever, J., Jervis, D., Durak, B. O. A., Xia, Y., and Huang, Y.: Quantifying

717   methane point sources from fine-scale satellite observations of atmospheric methane plumes, Atmos.

718   Meas. Tech., 11, 5673-5686, https://amt.copernicus.org/articles/11/5673/2018/, 2018.

719   Vaughn, T. L., Bell, C. S., Pickering, C. K., Schwietzke, S., Heath, G. A., Pétron, G., Zimmerle, D. J.,

720   Schnell, R. C., and Nummedal, D.: Temporal variability largely explains top-down/bottom-up difference

721   in methane emission estimates from a natural gas production region, PNAS, 115, 11712-11717,

722   https://www.pnas.org/doi/abs/10.1073/pnas.1805687115, 2018.

723   Vinković, K., Andersen, T., de Vries, M., Kers, B., van Heuven, S., Peters, W., Hensen, A., van den Bulk,

724   P., and Chen, H.: Evaluating the use of an Unmanned Aerial Vehicle (UAV)-based active AirCore system

725   to quantify methane emissions from dairy cows, Sci. Total Environ., 831, 154898,

726   https://doi.org/10.1016/j.scitotenv.2022.154898, 2022.

727   Wecht, K. J., Jacob, D. J., Sulprizio, M. P., Santoni, G. W., Wofsy, S. C., Parker, R., Bösch, H., and

728   Worden, J.: Spatially resolving methane emissions in California: constraints from the CalNex aircraft

729   campaign and from present (GOSAT, TES) and future (TROPOMI, geostationary) satellite observations,

730   Atmos. Chem. Phys., 14, 8173-8184, https://acp.copernicus.org/articles/14/8173/2014/, 2014.

731   Zhang, Y., Gautam, R., Pandey, S., Omara, M., Maasakkers, J. D., Sadavarte, P., Lyon, D., Nesser, H.,

732   Sulprizio, M. P., Varon, D. J., Zhang, R., Houweling, S., Zavala-Araiza, D., Alvarez, R. A., Lorente, A.,

733   Hamburg, S. P., Aben, I., and Jacob, D. J.: Quantifying methane emissions from the largest oil-producing

734   basin in the United States from space, *Sci. Adv.*, 6, eaaz5120,

735   https://www.science.org/doi/abs/10.1126/sciadv.aaz5120, 2020.

736   Zinchenko, A. V., Paramonova, N. N., Privalov, V. I., and Reshetnikov, A. I.: Estimation of methane

737   emissions in the St. Petersburg, Russia, region: An atmospheric nocturnal boundary layer budget

738   approach, J. Geophys. Res-Atmos., 107, ACH 2-1-ACH 2-11, https://doi.org/10.1029/2001JD001369,

739   2002.

740